The 2018 Fiji M_w 8.2 and 7.9 deep earthquakes: One doublet in two slabs

Zhe Jia [a], Zhichao Shen [a], Zhongwen Zhan [a,*], Chenyu Li [b], Zhigang Peng [b], Michael Gurnis [a]

[a] *Seismological Laboratory, California Institute of Technology, Pasadena, CA 91125, USA*
[b] *School of Earth and Atmospheric Sciences, Georgia Institute of Technology, Atlanta, GA 30332, USA*

A B S T R A C T

The cold Fiji-Tonga subduction zone accounts for >75% of cataloged deep earthquakes but none of the largest ten in the last century. On 19 August 2018 and 06 September 2018, a deep earthquake doublet with moment magnitude (M_w) 8.2 and 7.9 struck the Fiji area, providing a rare opportunity to interrogate the behaviors of great deep earthquakes in cold slabs. While the aftershock productivity of the 2018 M_w 8.2 event is similar to the 2013 Okhotsk M_w 8.3 event in a cold slab, the inferred compact rupture dimensions of both the M_w 8.2 and 7.9 events appear to be similar to the 1994 Bolivia earthquake in a warm slab. This seems to contradict the traditional view that slab temperature controls deep earthquakes. However, we find that neither event was confined within the cold Tonga slab core: the M_w 8.2 ruptured mostly in the warmer rim of the Tonga slab and the M_w 7.9 occurred in a warm relic slab leaning on top of the Tonga slab. The Fiji doublet demonstrates local slab temperature as the critical factor for deep earthquakes, and reveals complex interaction of subducted slabs in Tonga.

© 2019 Elsevier B.V. All rights reserved.

1. Introduction

Since the discovery of deep earthquakes below 300 km in the 1920s, the Fiji-Tonga subduction zone has produced more than 75% of global deep seismicity above magnitude 4, but none of the ten largest deep earthquakes (Houston, 2015). This deficit of large events is reflected in Fiji-Tonga's higher Gutenberg-Richter b value than in other subduction zones (Wiens and Gilbert, 1996; Zhan, 2017), and was commonly attributed to its colder slab with older incoming plate and faster plate convergence (Wiens and Gilbert, 1996; Wiens, 2001). On August 19th, 2018, the first instrumentally recorded $M > 8$ Fiji deep earthquake occurred (Fig. 1A), with a centroid depth of 556 km (Fig. S1) and a moment magnitude (M_w) 8.2, slightly smaller than the 1994 Bolivia M_w 8.2 earthquake, the second largest deep earthquake after the 2013 Okhotsk M_w 8.3 earthquake (Table S1). The M_w 8.2 Fiji event produced hundreds of aftershocks, elevating seismic activity within a few hundred kilometers. On September 6th, a M_w 7.9 earthquake occurred about 250 km to the west at 655 km depth (Fig. S1), being the second largest deep earthquake in the Fiji-Tonga region. Background seismicity in the M_w 7.9 source area had been minimal but increased substantially since the M_w 8.2 earthquake (Fig. 1B). Pre-

sumably, the M_w 8.2 event triggered the M_w 7.9, forming the first magnitude 8 (M8) deep earthquake doublet (Tibi et al., 2003b; Ye et al., 2016).

The Fiji deep doublet and their aftershocks provide a unique opportunity to test our understanding of the still enigmatic deep earthquake mechanism, especially the properties of great deep earthquakes in cold slabs. The primary control on deep earthquakes appears to be slab temperature, which is often represented by the thermal parameter $\phi = a * v * \sin\theta$, where θ is slab dip, a is incoming plate age, and v is plate convergence rate (Kirby et al., 1991; Wiens and Gilbert, 1996). Deep earthquakes have only been detected in subduction zones with ϕ above 2000 km, and the maximum depths of earthquakes increase monotonically with ϕ (Gorbatov et al., 1997). In addition to the aforementioned b-value difference, deep earthquakes in cold slabs are substantially more productive in aftershocks than those in warm slabs (Wiens and Gilbert, 1996). Rupture processes of large deep earthquakes also show systematic dependence on slab temperature (Tibi et al., 2003a). For example, the 2013 Okhotsk M_w 8.3 earthquake in the cold Kuril subduction zone ($\phi \sim 6000$ km) had higher rupture speed, lower stress drop, and higher seismic radiation efficiency (i.e., lower dissipation) than the 1994 Bolivia M_w 8.2 event in the warm South America subduction zone ($\phi \sim 2000$ km) (Zhan et al., 2014). Large deep earthquakes in the cold Fiji-Tonga subduction zone ($\phi \sim 8000$ km) may then be expected to be more brittle in rupture, more efficient in seismic energy radiation, and to pro-
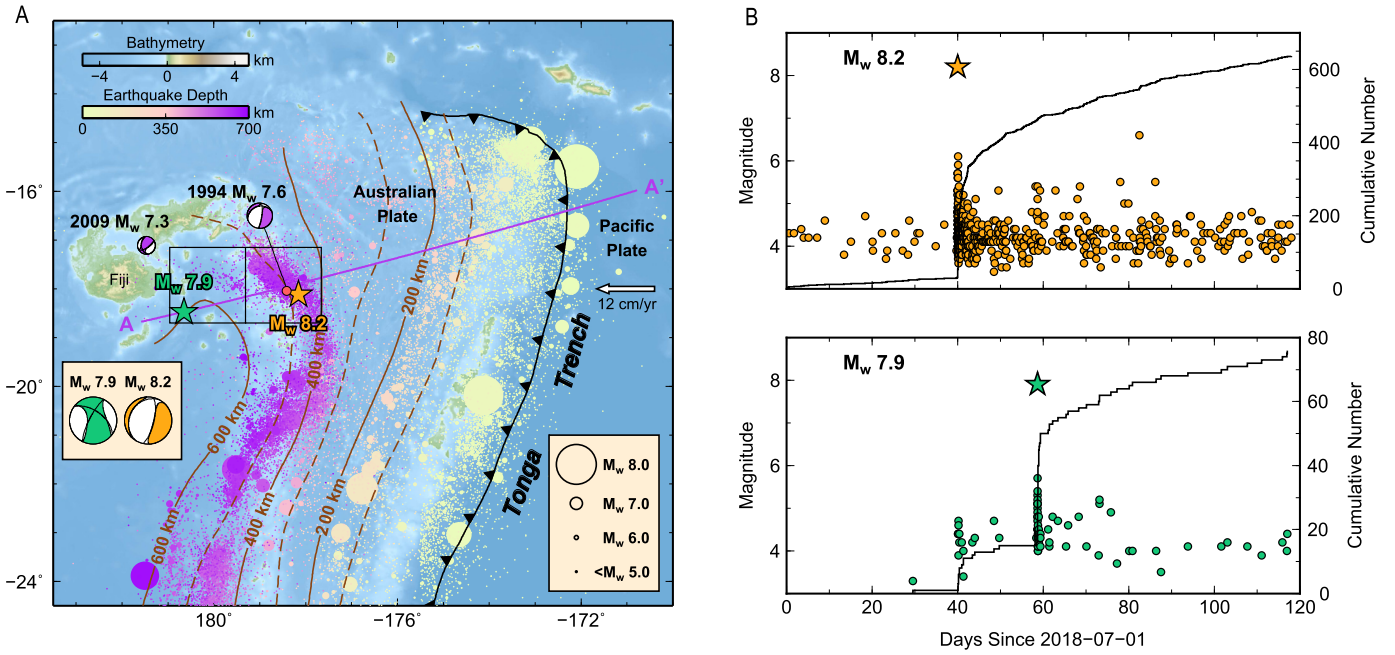
A

B

Fig. 1. Tectonic setting and seismicity. (A) The 2018 Fiji deep earthquake doublet (M_w 8.2 and M_w 7.9) occurred in the northern end of Fiji-Tonga subduction zone where the Pacific plate subducts under the Australian plate, as illustrated by the background seismicity (dots) based on the ISC catalog and the slab depth contours from the Slab 2.0 model (Hayes et al., 2018). The stars show the mainshock epicenter locations, and the mainshock moment tensors from Global CMT catalog are displayed in the inset. (B) Seismic activity around the M_w 8.2 and M_w 7.9 events in the black squares in (A) based on the ISC catalog. Body wave magnitudes are plotted except for the mainshocks. Solid black lines denote the cumulative number of aftershock in the mainshock regions (boxes in A). The M_w 8.2 event triggered hundreds of aftershocks near its rupture area and also elevated activity in the source region of the later M_w 7.9 event, during the three weeks in between. The M_w 7.9 event produced another tens of aftershocks around its rupture area.

duce more aftershocks. To evaluate these properties, we analyze the source processes of the 2018 Fiji doublet through modeling of seismic observations, and compare their rupture properties, aftershock productivities and thermal environments with previous large deep earthquakes.

2. Rupture properties of the Fiji doublet

In this section, we estimate the radiated seismic energy of the Fiji doublet based on body-wave magnitudes (m_B), determine focal mechanisms of their initial ruptures through P-wave first-motion polarities, and image the rupture processes through subevent inversion of globally observed seismograms.

2.1. Radiated seismic energy and radiation efficiency

Here we use an empirical approach that converts global estimates of body wave magnitude m_B to radiated energy E_R (Gutenberg and Richter, 1956; Kanamori and Ross, 2018). We use teleseismic (from 30° to 80°) vertical component seismograms on the Global Seismic Network (GSN) and the international Federation of Digital Seismograph Networks (FDSN) stations from IRIS DMC (Incorporated Research Institutions for Seismology Data Management Center) to estimate the body-wave magnitude m_B. After removing the instrumental responses, we convolve the displacement seismograms with the Wiechert-type instrumental response. Then, we measure the P wave peak amplitude and period (T_p) and correct for the instrument gain at the period of the peak phase to determine the ground motion amplitude (A_p). The body-wave magnitude m_B at each station is calculated by

$$m_B = \log_{10}\left(\frac{A_p}{T_p}\right) + Q\left(\Delta, h\right) \tag{1}$$

where Q is an empirical function of epicentral distance Δ and earthquake depth h (Kanamori and Ross, 2018). The final body-wave magnitude is the median value of m_B from all stations. We related the body-wave magnitude m_B to radiated seismic energy E_R using an empirical equation (Gutenberg and Richter, 1956; Kanamori and Ross, 2018):

$$\log_{10} E_R = 5.8 + 2.4 m_B \tag{2}$$

where E_R is in ergs. Kanamori and Ross (2018) verified the accuracy of the above equation by comparing with previous radiated energy estimates and found differences within a factor of two for deep earthquakes. Once the radiated seismic energy is obtained, the scaled energy can be computed with E_R/M_0, where M_0 is the seismic moment from the Global CMT catalog (www.globalcmt.org).

We find that the radiated energy estimates for the Fiji doublet are not substantially higher than for previous M8 deep earthquakes: 1.29×10^{24} ergs and 2.31×10^{23} ergs for the M_w 8.2 and M_w 7.9 earthquakes, respectively (Table 1). In comparison, our estimated E_R for the 1994 Bolivia and the 2013 Okhotsk earthquakes are 1.42×10^{24} ergs and 1.72×10^{24} ergs, consistent with previous

Table 1

Comparison of body-wave magnitude (m_B), radiated energy, and scaled energy of the six large deep earthquakes discussed in this study. Numbers in red are from Kanamori and Ross (2018) as comparisons.

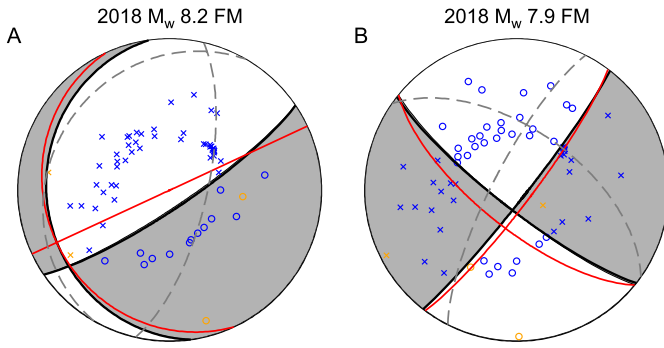|	Body wave magnitude (m_B)	Radiated energy (Erg)	Scaled radiated energy (10^{-5})
1994 Fiji M_w 7.5	7.17 (7.16)	1.03×10^{23}	3.35 (3.14)
1994 Bolivia M_w 8.2	7.65 (7.65)	1.42×10^{24}	5.41 (5.53)
2013 Okhotsk M_w 8.3	7.68 (7.69)	1.72×10^{24}	4.34 (4.47)
2015 Bonin M_w 7.9	7.35 (7.37)	2.72×10^{23}	3.56 (4.09)
2018 Fiji M_w 8.2	7.63	1.29×10^{24}	4.89
2018 Fiji M_w 7.9	7.32	2.31×10^{23}	2.68

Fig. 2. First-motion focal mechanisms for (A) the M_w 8.2 and (B) the M_w 7.9 events. Blue circles and crosses respectively indicate the positive and negative polarities from teleseismic seismograms. Orange circles and crosses respectively indicate the positive and negative polarities from regional seismograms. Dashed fault planes denote the best-fitting double-couple focal mechanisms based on the GCMT solutions. The solid fault planes are the first-motion solutions (strike, dip), (172°, 20°) and (56°, 80°) for the M_w 8.2 event, and (38°, 85°) and (128°, 80°) for the M_w 7.9 event. Red lines indicate first subevent focal mechanisms from the subevent rupture models inverted from seismic waveforms (Fig. 3). (For interpretation of the colors in the figure(s), the reader is referred to the web version of this article.)

measurements (Kanamori et al., 1998; Ye et al., 2013). After normalization by their seismic moments M_0, there is no substantial difference in the scaled energy E_R/M_0 for all four events (Table 1), given the uncertainties of E_R. Therefore, the Fiji events, although in the world's coldest subduction zone, did not radiate more seismic energy than events in warmer subduction zones. Further comparison of radiation efficiency $\eta_R = E_R/\Delta W_0$ requires estimating the available strain energy $\Delta W_0 = M_0 \Delta\sigma/2\mu$, and stress drop $\Delta\sigma \propto M_0/L^3$ is highly sensitive to the earthquake rupture dimension L. Hence, to quantify whether the Fiji doublet are more seismically efficient than previous large deep earthquakes in warmer subduction zones, we need to constrain the rupture dimensions of these earthquakes consistently.

2.2. First-motion focal mechanisms

To gain insights on possible ruptures complexities, we first investigate the initiations of the Fiji doublet ruptures, by examining their first-motion focal mechanisms relative to the centroid moment tensors. We manually pick the first arrivals of broadband P waves on both regional and teleseismic stations, identify their polarities, and determine the geometries of nodal planes. Fig. 2 shows the observed P-wave polarities and the estimated first-motion mechanisms (solid lines and shades), with substantial differences from the best-fitting double-couple mechanisms based on the Global CMT solutions (dashed lines). For the M_w 8.2 earthquake, the difference in focal mechanism (strike/dip of 56°/80° vs. 13°/70°) is mostly due to the positive polarities observed at stations to the southwest (SW) directions (Fig. 2A). Polarity observations of the M_w 7.9 earthquake indicate a strike-slip mechanism, with two nodal planes of strike/dip = 38°/85° and 128°/80°, both of which deviate substantially from the double-couple component of the Global CMT solution (strike/dip = 305°/57° and 207°/77°) (Fig. 2B). The differences between the first-motion mechanisms and the centroid mechanisms indicate substantial changes in fault geometry or rake angle during the ruptures of the Fiji doublet, which we accommodate in the subevent inversions.

2.3. Rupture processes and aftershocks

We image the doublet rupture processes and dimensions by subevent inversions. Our subevent inversion method parameterizes a large earthquake as a series of point sources (subevents) and uses

teleseismic P, SH, and pP waveforms to constrain properties of individual subevents. It is similar to a previous method applied to the 1994 Bolivia and 2013 Okhotsk earthquakes (Zhan et al., 2014), but includes subevent focal mechanisms explicitly to quantify changes of radiation pattern along rupture. Furthermore, pP depth phases added to the inversion help resolve possible variations in subevent depths. In this method, we invert for the centroid locations, centroid times, durations, and moment tensors of all subevents. Our method combines non-linear inversion for a subset of parameters and linear inversion for the rest. We apply Markov Chain Monte Carlo (MCMC) method to sample the posterior Probability Density Functions (PDFs) of the nonlinear parameters including the timings, locations, and durations of subevents. For a given set of subevent timings, locations, and durations (i.e., one MCMC sample), we evaluate the apparent source time function for each station, and linearly invert the seismic data for the subevent moment tensors. The data misfit from the set of nonlinear parameters and the corresponding moment tensor solutions is then used to estimate the probability in the MCMC inversion. Compared with a fully non-linear inversion scheme, this hybrid approach requires much less computation to search the parameter space, hence provides more robust solutions. The number of subevents increases iteratively until the waveforms are fit well. More details of our subevent method can be found in the supplementary material.

The subevent model for the M_w 8.2 earthquake (Fig. 3A, Fig. S2, Table S2) shows two stages of rupture. The first stage includes subevent E1 (centroid time $\tau_C = 8.15$ s, M_w 7.55), E2 ($\tau_C = 10.88$ s, M_w 7.66), and E3 ($\tau_C = 13.16$ s, M_w 7.61), aligned approximately in the NE direction with similar focal mechanisms (average strike/dip/rake = 43°/84°/−77°, 160°/18°/−152°). E1's focal mechanism from waveform inversion confirms the first-motion polarities of teleseismic P waves (Fig. 2A). Posterior Probability Density Functions (PDFs) of the subevent depths suggest that E3 is about 15 km shallower than E1 and E2 (Fig. S3), preferring the stage 1 rupture to be on the steep NE-strike fault plane (strike/dip = 43°/84°), which is also supported by the nearly vertical band of aftershocks (Fig. 4A). The largest subevent of stage 1, E2, appears to have triggered large slip on multiple faults in stage 2. Subevents E4 ($\tau_C = 14.88$ s, M_w 7.81), E5 ($\tau_C = 17.47$ s, M_w 7.72) and E6 ($\tau_C = 20.81$ s, M_w 7.83) are aligned towards the northwest (NW) and they have relatively similar focal mechanisms (average strike/dip/rake = 3°/71°/−100°, 213°/23°/−63°). The difference in radiation pattern between the two stages (Fig. 2A) is evident on the teleseismic P-wave displacement seismograms with flipping polarities (Fig. 3B, Fig. S4). Posterior PDFs suggest that E2, E4, E5, and E6 rupture sequentially towards shallower depths by about 30 km (Fig. 4B, Fig. S3), rejecting the shallow west-dipping nodal plane (strike/dip = 213°/23°) as the rupture plane. Furthermore, as E2, E4, E5, and E6 centroid locations are not aligned in the north-south (N–S) direction, it is also unlikely that they occurred on the N–S striking, steep fault plane (strike/dip = 3°/71°). This disagreement between the subevent strikes and the alignment of their locations is also confirmed by a simpler three-subevent model (Fig. 5), in which the two main subevents E2 and E3 are aligned from SE to NW, being located shallower, while their strikes are north. Therefore, we conclude that the stage 2 rupture must involve multiple faults, although the exact geometry is uncertain (e.g., en echelon vs. perpendicular faults). Previous magnitude 7 deep earthquakes in Fiji-Tonga show a diversity of fault geometries (Warren et al., 2007). The sum of the subevent moment tensors explains the long period moment tensor solution of the M_w 8.2 earthquake well, including the ∼10% non-double-couple (non-DC) component (Fig. S2). The overall subevent dimension of stage 2 is ∼30 km, about the same as stage 1 but with much larger total moment. The two stages altogether contribute to a total rupture dimension of ∼50 km, consistent with the three-subevent model
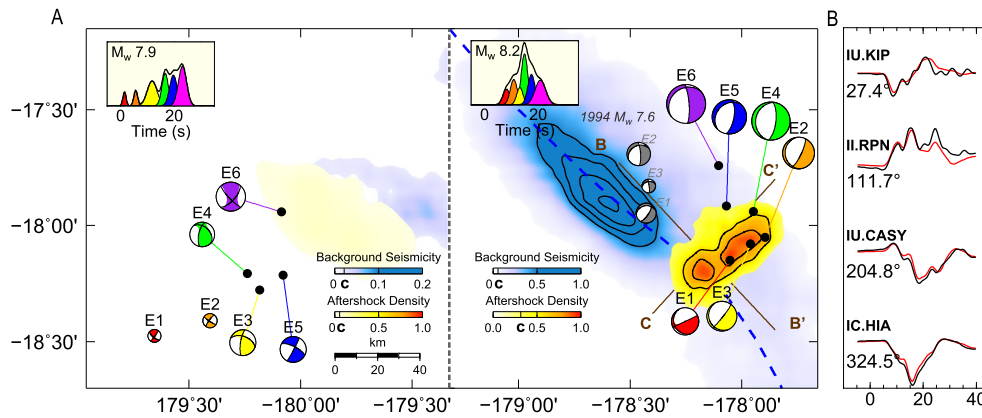
Fig. 3. Rupture processes of the 2018 Fiji doublet. (A) Subevent models for the M_w 7.9 (left half) and the M_w 8.2 events (right half). The black dots are centroid locations of the subevents, whose moment rate functions (MRFs) are shown in the inset with the same colors as their moment tensor beach balls. Density contours of relocated aftershocks are plotted over the contours of background seismicity based on the USGS NEIC catalog. They are displayed with different color scales and truncations ("C" on the colorbars if not 0). The M_w 8.2 event initiated near the slab center (blue dashed curve as inferred from the maximum background seismicity), but ruptured mostly 30 km to the NE by subevent E2, and E4-E6. Grey beachballs are subevent model of the 1994 Fiji M_w 7.6 earthquake. (B) Representative displacement waveform fits for the subevent model of the M_w 8.2 event at different azimuths, with data in black and synthetics in red. Early and late parts of the waveforms have opposite polarities at KIP and CASY, suggesting different focal mechanisms along the rupture.
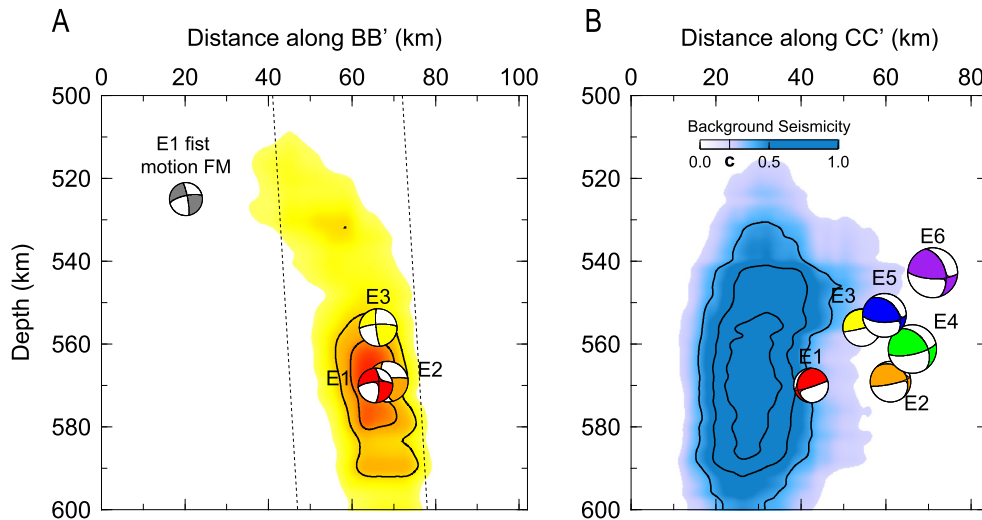

Fig. 4. Relation of the M_w 8.2 subevents with aftershocks and background seismicity. (A) Cross section along BB' in Fig. 3A showing the aftershocks of M_w 8.2 event extend nearly vertically, favoring the NE-strike fault plane for stage 1. Density contours of aftershocks are displayed with same color scale as in Fig. 3A. (B) Cross section along CC' in Fig. 3A showing the M_w 8.2 subevents spread by 30 km vertically and mostly away from the cold core as inferred from the background seismicity density.

(Fig. 5). To further confirm whether the estimation of rupture dimension is insensitive to our specific subevent parameterization and choice of number of subevents, we conduct another inversion approximating the earthquake as a single Haskell source. The result is a unilateral rupture towards the NW with a length close to 60 km, roughly consistent with the values from subevent inversions. However, the Haskell source model cannot capture the distribution of moment along rupture, or the changes in depth and moment tensor.

The M_w 8.2 earthquake produced over 400 $M > 4$ aftershocks during the following 80 days, more than any previous deep earthquake. In comparison, the 2013 Okhotsk and 1994 Bolivia earthquakes produced 71 and 4 $M > 4$ aftershocks in the same duration, respectively. After correcting for differences in catalog completeness and mainshock magnitudes (Utsu and Ogata, 1995; Peng et al., 2007), the aftershock productivity of the 2018 Fiji M_w 8.2 is similar to the 1994 Fiji M_w 7.6 earthquake, and significantly higher than other large deep earthquakes (Fig. 6). However, the distribution of the Fiji M_w 8.2 aftershocks is non-uniform and does not follow the mainshock slip distribution. Here we relocate the M_w 8.2 main shock and its aftershock using a teleseismic double dif-

ference algorithm (Pesicek et al., 2010). More details can be found in the supplementary materials. The aftershocks concentrated in a NE-strike band, aligned with the inferred fault plane for the stage 1 rupture but are sparser around the stage 2 rupture (Figs. 3A, 4A; Figs. S8–S9), which accounts for most of the total moment. This suggests that the aftershock productivities of the two stages of the M_w 8.2 are substantially different.

The M_w 7.9 event of the Fiji doublet has ∼30% non-doublecouple (non-DC) component in the USGS WPhase and the Global CMT solutions, compared with ∼10% for the M_w 8.2 event. This large non-DC is reflected by the diverse subevent focal mechanisms we derived from waveforms (Fig. 3A, Figs. S10–S13, Table S3), and supported by the deviation of polarity-based focal mechanism from the best-fitting double-couple of the Global CMT solution (Fig. 2). The earthquake first ruptured to the east (E1–E2), then the major subevents (E3 to E6) occurred in a cluster from SW to NE direction (Fig. 3A). Given the uncertainty of subevent locations and focal mechanisms, it is unclear whether they ruptured on a single NE-strike fault plane or as a cascade of ruptures on multiple faults (Fig. S10). By including both teleseismic depth phases (pP) and the up-going direct P and SH waveforms recorded by
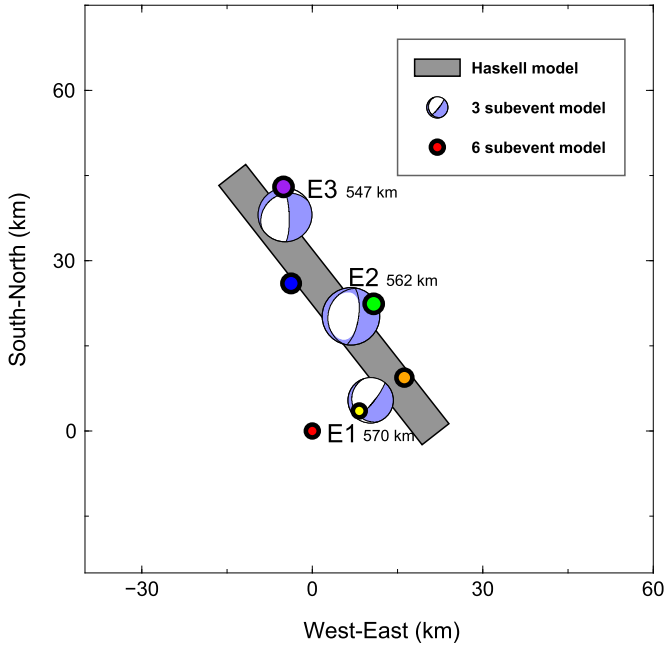
Fig. 5. Subevent models of different complexity for the M_w 8.2 event. The Haskell model, three-subevent model, and six-subevent model are indicated by the rectangle, beachballs and circles, respectively. Centroid depths of subevents for the three-subevent model are displayed. These models of different levels of complexity reveal consistent overall dimension and directivity of the earthquake. The three-subevent model captures the changes in focal mechanisms along rupture, but not the NE strike within the first stage. Therefore, we conclude that our preferred six-subevent model does not cause artifacts due to over parameterization but still capture important features of the earthquake rupture processes. Details of the Haskell model and the 3-subevent model can be found in Figs. S6–S7.
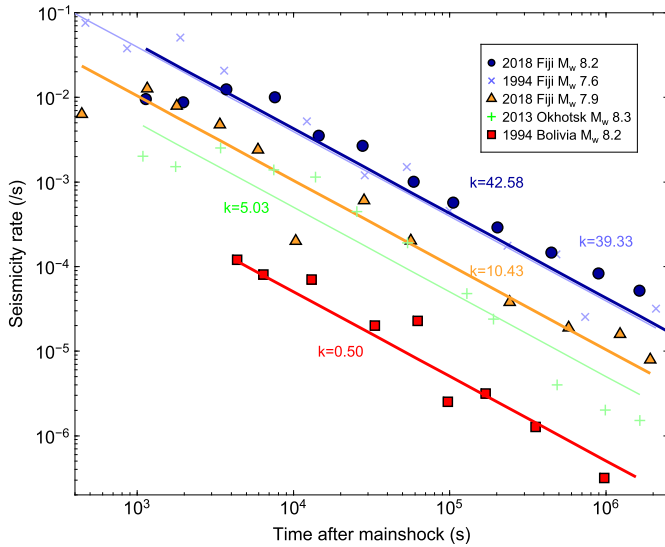

Fig. 6. Comparison of aftershock productivities of five large deep earthquakes. Aftershock seismicity rates as function of time for the 2018 Fiji doublet, the 1994 Bolivia and Fiji events, and the 2013 Okhotsk event based on the ISC and refined regional catalogs. The differences due to mainshock magnitude and catalog completeness have been corrected (see supplementary material for details). The aftershock catalog for the 1994 M_w 7.6 Fiji earthquake is from Wiens and McGuire (2000), and the 1994 M_w 8.2 Bolivian aftershocks are from Myers et al. (1995). The parameter k represents the aftershock productivity in the Omori law $n(t) = k/t^p$.

a local station MSVF in our inversion, we find that the M_w 7.9 event ruptured a 20 km depth range (Figs. S11–S14). The largest four subevents from E3 to E6 account for ~90% of the total moment and are concentrated within 40 km from each other laterally

(Fig. 3A), comparable to the subevent dimension of the M_w 8.2 event's stage 2 rupture.

3. Implications for temperature dependence of deep earthquakes

The rupture dimensions of the Fiji doublet from our subevent models seem to contradict the expectation of higher radiation efficiency for large deep earthquakes in a cold subduction zone. Fig. 7 displays five large deep earthquakes' subevent models at the same scale, all derived from consistent methodology for comparison. The Fiji doublet's rupture dimensions are similar to that of the 1994 Bolivia earthquake in the warm South American subduction zone and substantially smaller than the 2013 Okhotsk earthquake in the cold Kuril subduction zone. With E_R/M_0 for all these large deep earthquakes being similar to each other (Table 1), the radiation efficiency (η_R) estimates depend strongly on the rupture dimensions (L), $\eta_R \propto \Delta\sigma^{-1} \propto L^3/M_0$. However, both the M_w 8.2 and the M_w 7.9 Fiji events may have ruptured more than one fault, which makes the definition of rupture dimension or even the applicability of the stress drop scaling $\Delta\sigma \propto M_0/L^3$ questionable. Furthermore, the rupture dimensions on individual faults are poorly constrained without clear subevent directivity. This is a fundamental limitation of observing the sources from far field. Nevertheless, if we take the overall area in which subevents, especially the ones with the largest moments, are located as a proxy of the rupture dimension, the relatively compact rupture dimensions of the Fiji doublet suggest inefficient ruptures in terms of seismic radiation, despite being in the world's coldest subduction zone. This seems to contradict the view that slab temperature is the primary control on the rupture behaviors of deep earthquakes.

However, a more detailed comparison of the Fiji M_w 8.2 subevent model and the distribution of background seismicity suggest that the main rupture was not confined to the cold core of the Tonga slab, but occurred mostly in the warmer portion of the slab. Background deep seismicity is generally assumed to represent the cold brittle core of slabs (Antolik et al., 1999; Wiens, 2001). This assumption is supported by observations in areas with high-resolution tomography models and earthquake locations, such as the Japan subduction zone (Tao et al., 2018). In northern Fiji-Tonga, background seismicity forms a southeast (SE)-strike, steeply dipping band (Figs. 3A, 4B). Wiens et al. (1993) reported a deep double seismic zone with a refined regional catalog and further interpreted as top and bottom edges of a metastable olivine wedge in the cold slab core. They also noticed that the 1994 M_w 7.6 Fiji deep earthquake (Fig. 1A), ~40 km NW of the 2018 M_w 8.2 event, started within the background seismic band but ruptured outside the band to the north and northeast. We confirm this observation with our subevent model for the 1994 Fiji event, with a M_w 7.3 subevent E1 in the center of the seismic band and a M_w 7.4 subevent E2 towards northern edge of the band (Fig. 3A, Fig. 7, Table S4). The 2018 M_w 8.2 earthquake had a similar rupture process but was more complicated. It initiated near the center of the background seismicity band and ruptured on a nearly vertical fault perpendicular to the slab strike toward the northeast (NE), away from the slab core. The second stage of rupture (E2, E4~6), which accounts for most of the moment, all ruptured near the edge of the background seismic band, about 30 km away from the center line (Fig. 3). Thermal modeling of the subducted Tonga slab suggests that the temperature around the stage 2 rupture would be ~900 °C, 200 °C warmer than the center (Fig. 8B). This inferred temperature difference for the two rupture stages is also supported by the distribution of aftershocks, with most aftershocks around the lower-moment stage 1 near slab center (Fig. 3A). The temperature dependence of deep aftershock productivity has been observed in many subduction zones (Wiens and Gilbert, 1996), but
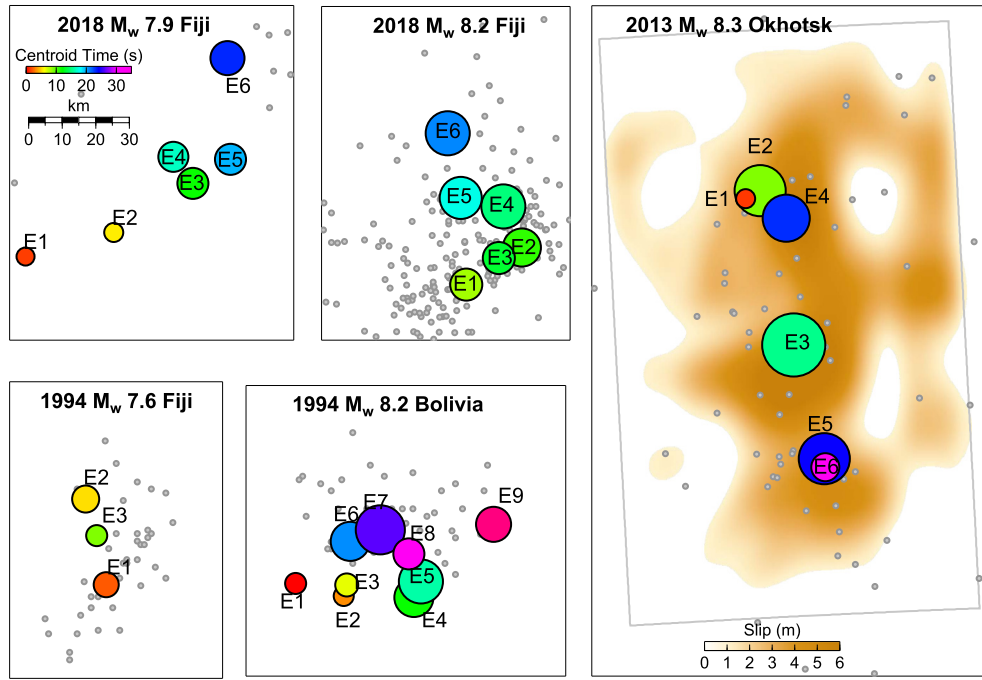
Fig. 7. Comparison of rupture dimensions of five large deep earthquakes. Subevent models of the five deep events in Fig. 5 plotted at the same length scale. Color of the circles indicates subevent centroid times and size represents subevent moment. Gray dots are the aftershocks in one month following the mainshocks. Subevents of the Okhotsk earthquake are plotted on top of a finite fault slip model (Wei et al., 2013).
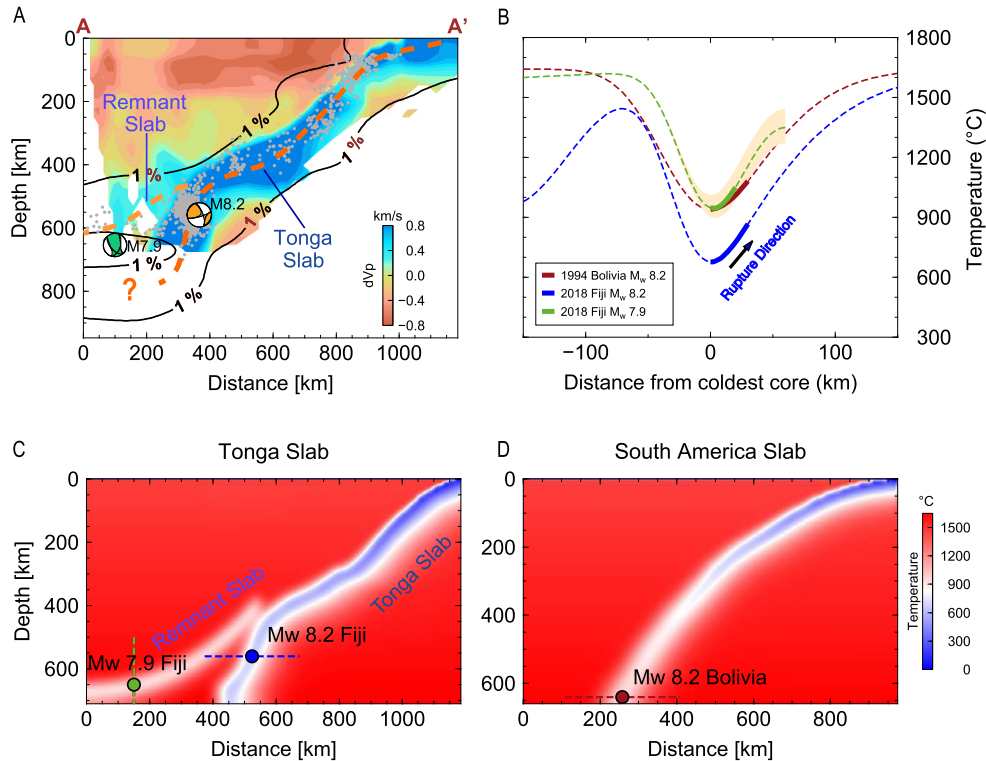

Fig. 8. Thermal modeling of the Fiji doublet. (A) Tomographic models along cross section AA' in Fig. 1A, showing the Fiji doublet with respect to the Tonga slab and the inferred remnant slab. The solid black lines are the 1% P wave velocity anomaly contours from the GAP model (Fukao and Obayashi, 2013). The background colors show the regional tomography model by Conder and Wiens (2006). The gray dots are the background seismicity. (B) Slab temperature profiles through three large deep earthquakes, whose approximate rupture extents are marked by thick line segments. Temperature uncertainty of the remnant slab is indicated by the shadow in light yellow. (C) Simulated thermal structure for the Tonga slab and the remnant slab. The dashed lines show the profiles in (B). (D) Same as (C) but for the South America slab.

is happening within the Fiji M_w 8.2 between the cold core and warm slab rim.

The M_w 7.9 earthquake, on the other hand, appears to occur within the relic Fiji slab, which is overall warmer than the adjacent Tonga slab. This event is a good example of so-called "isolated large deep earthquakes" that occur in region with little background seismicity and produce very few aftershocks (Lundgren and Giardini, 1994). The M_w 7.9 event produced much fewer

aftershocks than the M_w 8.2 earthquake (Fig. 6), especially if we only consider those within the mainshock rupture area (Fig. 7). Other examples of isolated events include the 1954 M_w 7.9 Spain, the 1970 M_w 8.0 Colombia, and the 2015 M_w 7.9 Bonin Islands earthquakes. It is proposed that isolated deep earthquakes occur in warm or remnant slabs that have difficulty nucleating spontaneously. But once started or triggered, isolated deep earthquakes can rupture and completely release the high stress accumulated over time, therefore leaving little residual stress for aftershocks (Kirby et al., 1996; Frohlich, 2006; Cai and Wiens, 2016). The 2018 M_w 7.9 Fiji earthquake occurred where the relic Fiji slab has been long inferred, based on seismicity/focal mechanisms, tomographic models, and geodynamic investigation of the tectonic history (Chen and Brudzinski, 2001; Brudzinski and Chen, 2003; Richards et al., 2011). In particular, both regional (Conder and Wiens, 2006) and global (Fukao and Obayashi, 2013) models show a high velocity zone above the Tonga slab (Fig. 8A). The 2009 M_w 7.3 Fiji deep earthquake (Fig. 1A) also triggered aftershocks that illuminated the normally aseismic relic slab (Cai and Wiens, 2016). The remnant slab presumably subducted from the initiation of the Vanuatu trench approximately 15 million years (Ma) ago (Seton et al., 2012). The consumed Australian plate would have been formed earlier by the rapid eastward migration of the Tonga subduction zone that initiated at ~50 Ma. Consequently, the lithosphere of the remnant slab would have been about ~35 Ma old (see supplementary material for details). Thermal modeling shows that the coldest core of such remnant slab would be ~1000 °C, similar to the warm South America slab and the warmer rim of the Tonga slab where the Fiji M_w 8.2 stage 2 rupture occurred (Figs. 8B–8D, Fig. S15). Therefore, we propose that the M_w 7.9 earthquake occurred in the relic Fiji slab. The agreements in temperature consistently explain the low background seismicity, compact subevent locations, and low aftershock productivity of the 1994 Bolivia M_w 8.2, 2018 Fiji M_w 7.9, and the stage 2 rupture of the 2018 Fiji M_w 8.2 events.

4. Discussion

Recently Fan et al. (2019) applied teleseismic back projection to the Fiji M_w 8.2 event and estimated that the rupture extended ~100 km to the north from the hypocenter, accompanied with changing focal mechanisms and rupture directions. Our source models of the M_w 8.2 event (Fig. 5) confirm the two-stage rupture with different directivity and the first stage on a vertical fault plane producing most of the aftershocks, consistent with Fan et al. (2019)'s result. However, the last subevent in our model is located ~50 km to the north of the hypocenter, indicating substantially more compact rupture dimension (50–60 km; Fig. 5) than the estimate of 110–150 km in Fan et al. (2019). This difference results in non-trivial difference in average stress drop and the temperature range of slab over which the M_w 8.2 event ruptured (Fig. S16). The sum of the six subevent moment tensors has a moment of 2.57×10^{28} dyne-cm, close to the Global CMT moment (2.52×10^{28} dyne-cm), suggesting that we are not missing any major subevent in our model. The difference in rupture dimension between our study and Fan et al. (2019) may be due to frequency dependent seismic radiation, as commonly observed for shallow megathrust earthquakes (Koper et al., 2011; Yao et al., 2013). Back projection method tracks the radiators of high-frequency energy, while the subevent inversion images the spatial distribution of seismic moment or slip. Therefore, a subevent with strong high-frequency radiation but low moment may be missed in our models.

Earthquakes are often assumed to rupture on a single fault, although in recent years more near field data and high-resolution aftershock patterns have revealed complicated faulting geometry for several large shallow earthquakes (e.g., 2012 Sumatra, 2016 Kaikoura) (Yue et al., 2012; Hamling et al., 2017). Resolving fault plane(s) for deep earthquakes with only far-field seismic data is challenging. In this paper, we take the discrepancy between subevent focal mechanisms and locations (Fig. 3, Fig. 5) in our subevent models of the Fiji M_w 8.2 earthquake as evidences for rupture over multiple faults during stage 2, though it is unclear how the rupture propagates/jumps though these faults. Another example of multiple-fault rupture of deep earthquakes was suggested by Chen et al. (2014), where they found the subevents of the 2013 Okhotsk M_w 8.3 earthquake cannot be fit onto a planar fault. This kind of rupture complexity challenges the conventional interpretation of deep earthquake properties. For example, an average rupture velocity estimated from either subevent modeling, teleseismic back-projection, or finite-fault inversion assuming a simplified fault geometry may not reflect the true source dynamics. The rupture velocity is defined by propagation of the rupture front, but one might approximate it by the subevent centroid migration speed instead. The centroidal rupture speeds V_{cr} of the M_w 8.2 event, considering the subevent depth variations, are about 4.5 km/s (Fig. S17) for both stages. However, we believe only the stage 1 V_{cr} is related to a continuous rupture on a vertical fault plane, and the relatively high speed is consistent with the interpretation that the M_w 8.2 event initiated in the cold slab core. On the other hand, because our far-field seismic data cannot resolve the rupture speeds of individual subevents, the stage 2 V_{cr} may represent static/dynamic triggering among subevents on different faults (Tibi et al., 2003b; Wei et al., 2013; Chen et al., 2014; Zhan and Shearer, 2014; Cai and Wiens, 2016). This dilemma also applies to the M_w 7.9 event, for which V_{cr} is ~3.1 km/s for the major subevents (Fig. S18) but we cannot define a clear fault plane. Therefore, the subevent rupture speeds of the doublet, which are more important than V_{cr} for the estimation of stress drops and radiation efficiency, are not well constrained and need further investigations.

5. Conclusions

In summary, the 2018 Fiji doublet reflects the complex interaction of slabs near the bottom of the mantle transition zone. The relic Fiji slab sank through the mantle wedge, with one end leaning onto the underlying Tonga slab and deforming the cold/brittle Tonga slab core, producing excessive amount of deep seismicity and a local rotation of stress. Meanwhile, the warm relic Fiji slab is under sub-horizontal compression, but has difficulty nucleating and releasing the stress seismically due to the lack of a brittle cold core. Most previous deep earthquakes in the Tonga slab are confined to the brittle core, or only rupture partially outside in some of the larger events (e.g., 1994 Fiji M_w 7.6). The 2018 M_w 8.2 event triggered large and complex ruptures in the warmer portion of slab and generated strong static/dynamic stress perturbations in the surrounding area, including the relic Fiji slab. Three weeks later, one of the triggered events in the relic slab succeeded in cascading into a M_w 7.9 event and released the high stress accumulated over time. Although the Fiji doublet occurred in the world's coldest subduction zone, neither was confined to the cold core of the Tonga slab. Therefore, their unexpected behaviors in terms of rupture dimension, radiation efficiency, and aftershocks support, not contradict, the traditional view that temperature is the main control on deep earthquakes. This emphasizes the importance of detailed mapping of deep earthquake ruptures along with the thermal structure implied by the tectonic evolution of the margin.

Acknowledgements

Appendix A. Supplementary material

Supplementary material related to this article can be found online at https://doi.org/10.1016/j.epsl.2019.115997.

References

Antolik, M., Dreger, D., Romanowicz, B., 1999. Rupture processes of large deep-focus earthquakes from inversion of moment rate functions. J. Geophys. Res. 104, 863–894.

Brudzinski, M.R., Chen, W.P., 2003. A petrologic anomaly accompanying outboard earthquakes beneath Fiji-Tonga: corresponding evidence from broadband P and S waveforms. J. Geophys. Res., Solid Earth 108, B6.

Cai, C., Wiens, D.A., 2016. Dynamic triggering of deep earthquakes within a fossil slab. Geophys. Res. Lett. 43, 9492–9499.

Chen, W.P., Brudzinski, M.R., 2001. Evidence for a large-scale remnant of subducted lithosphere beneath Fiji. Science 292, 2475–2479.

Chen, Y., Wen, L., Ji, C., 2014. A cascading failure during the 24 May 2013 great Okhotsk deep earthquake. J. Geophys. Res. 119, 3035–3049.

Conder, J.A., Wiens, D.A., 2006. Seismic structure beneath the Tonga arc and Lau back-arc basin determined from joint Vp, Vp/Vs tomography. Geochem. Geophys. Geosyst. 7, 3.

Fan, W., Wei, S.S., Tian, D., McGuire, J.J., Wiens, D.A., 2019. Complex and diverse rupture processes of the 2018 M_w 8.2 and M_w 7.9 Tonga-Fiji deep earthquakes. Geophys. Res. Lett. 46, 2434–2448.

Frohlich, C., 2006. Deep Earthquakes. Cambridge University Press, Cambridge, UK.

Fukao, Y., Obayashi, M., 2013. Subducted slabs stagnant above, penetrating through, and trapped below the 660 km discontinuity. J. Geophys. Res. 118, 5920–5938.

Gorbatov, A., Kostoglodov, V., Suárez, G., Gordeev, E., 1997. Seismicity and structure of the Kamchatka subduction zone. J. Geophys. Res., Solid Earth 102, 17883–17898.

Gutenberg, B., Richter, C.F., 1956. Earthquake magnitude, intensity, energy, and acceleration: (second paper). Bull. Seismol. Soc. Am. 46, 105–145.

Hamling, I.J., Hreinsdóttir, S., Clark, K., Elliott, J., Liang, C., Fielding, E., Litchfield, N., Villamor, P., Wallace, L., Wright, T.J., 2017. Complex multifault rupture during the 2016 M_w 7.8 Kaikōura earthquake, New Zealand. Science 356, eaam7194.

Hayes, G.P., Moore, G.L., Portner, D.E., Hearne, M., Flamme, H., Furtney, M., Smoczyk, G.M., 2018. Slab2, a comprehensive subduction zone geometry model. Science 362, 58–61.

Houston, H., 2015. Deep Earthquakes, pp. 329–354.

Kanamori, H., Anderson, D.L., Heaton, T.H., 1998. Frictional melting during the rupture of the 1994 Bolivian earthquake. Science 279, 839–842.

Kanamori, H., Ross, Z.E., 2018. Reviving mB. Geophys. J. Int. 216, 1798–1816.

Kirby, S.H., Durham, W.B., Stern, L.A., 1991. Mantle phase changes and deep-earthquake faulting in subducting lithosphere. Science 252, 216–225.

Kirby, S.H., Stein, S., Okal, E.A., Rubie, D.C., 1996. Metastable mantle phase transformations and deep earthquakes in subducting oceanic lithosphere. Rev. Geophys. 34, 261–306.

Koper, K.D., Hutko, A.R., Lay, T., Ammon, C.J., Kanamori, H., 2011. Frequency-dependent rupture process of the 2011 M_w 9.0 Tohoku earthquake: comparison of short-period P wave backprojection images and broadband seismic rupture models. Earth Planets Space 63, 16.

Lundgren, P., Giardini, D., 1994. Isolated deep earthquakes and the fate of subduction in the mantle. J. Geophys. Res. 99, 15833.

Myers, S.C., Wallace, T.C., Beck, S.L., Silver, P.G., Zandt, G., Vandecar, J., Minaya, E., 1995. Implications of spatial and temporal development of the aftershock sequence for the M_w 8.3 June 9, 1994 deep Bolivian earthquake. Geophys. Res. Lett. 22, 2269–2272.

Peng, Z., Vidale, J.E., Ishii, M., Helmstetter, A., 2007. Seismicity rate immediately before and after main shock rupture from high-frequency waveforms in Japan. J. Geophys. Res., Solid Earth 112, B3.

Pesicek, J., Thurber, C., Zhang, H., DeShon, H., Engdahl, E., Widiyantoro, S., 2010. Teleseismic double-difference relocation of earthquakes along the Sumatra-Andaman subduction zone using a 3-D model. J. Geophys. Res., Solid Earth 115, B10.

Richards, S., Holm, R., Barber, G., 2011. When slabs collide: a tectonic assessment of deep earthquakes in the Tonga-Vanuatu region. Geology 39, 787–790.

Seton, M., Müller, R., Zahirovic, S., Gaina, C., Torsvik, T., Shephard, G., Talsma, A., Gurnis, M., Turner, M., Maus, S., 2012. Global continental and ocean basin reconstructions since 200 Ma. Earth-Sci. Rev. 113, 212–270.

Tao, K., Grand, S.P., Niu, F., 2018. Seismic structure of the upper mantle beneath Eastern Asia from full waveform seismic tomography. Geochem. Geophys. Geosyst. 19, 2732–2763.

Tibi, R., Bock, G., Wiens, D.A., 2003a. Source characteristics of large deep earthquakes: constraint on the faulting mechanism at great depths. J. Geophys. Res. 108, 2091.

Tibi, R., Wiens, D.A., Inoue, H., 2003b. Remote triggering of deep earthquakes in the 2002 Tonga sequences. Nature 424, 921–925.

Utsu, T., Ogata, Y., 1995. The centenary of the Omori formula for a decay law of aftershock activity. J. Phys. Earth 43, 1–33.

Warren, L.M., Hughes, A.N., Silver, P.G., 2007. Earthquake mechanics and deformation in the Tonga-Kermadec subduction zone from fault plane orientations of intermediate-and deep-focus earthquakes. J. Geophys. Res., Solid Earth 112, B5.

Wei, S., Helmberger, D., Zhan, Z., Graves, R., 2013. Rupture complexity of the M_w 8.3 sea of Okhotsk earthquake: rapid triggering of complementary earthquakes? Geophys. Res. Lett. 40, 5034–5039.

Wiens, D.A., 2001. Seismological constraints on the mechanism of deep earthquakes: temperature dependence of deep earthquake source properties. Phys. Earth Planet. Inter. 127, 145–163.

Wiens, D.A., Gilbert, H.J., 1996. Effect of slab temperature on deep-earthquake aftershock productivity and magnitude-frequency relations. Nature 384, 153–156.

Wiens, D.A., McGuire, J.J., 2000. Aftershocks of the March 9, 1994, Tonga earthquake: the strongest known deep aftershock sequence. J. Geophys. Res., Solid Earth 105, 19067–19083.

Wiens, D.A., McGuire, J.J., Shore, P.J., 1993. Evidence for transformational faulting from a deep double seismic zone in Tonga. Nature 364, 790–793.

Yao, H., Shearer, P.M., Gerstoft, P., 2013. Compressive sensing of frequency-dependent seismic radiation from subduction zone megathrust ruptures. Proc. Natl. Acad. Sci. 110, 4512–4517.

Ye, L., Lay, T., Kanamori, H., Koper, K.D., 2013. Energy release of the 2013 M_w 8.3 sea of Okhotsk earthquake and deep slab stress heterogeneity. Science 341, 1380–1384.

Ye, L., Lay, T., Kanamori, H., Zhan, Z., Duputel, Z., 2016. Diverse rupture processes in the 2015 Peru deep earthquake doublet. Sci. Adv. 2, e1600581.

Yue, H., Lay, T., Koper, K.D., 2012. En échelon and orthogonal fault ruptures of the 11 April 2012 great intraplate earthquakes. Nature 490, 245.

Zhan, Z., 2017. Gutenberg–Richter law for deep earthquakes revisited: a dual-mechanism hypothesis. Earth Planet. Sci. Lett. 461, 1–7.

Zhan, Z., Kanamori, H., Tsai, V.C., Helmberger, D.V., Wei, S., 2014. Rupture complexity of the 1994 Bolivia and 2013 sea of Okhotsk deep earthquakes. Earth Planet. Sci. Lett. 385, 89–96.

Zhan, Z., Shearer, P.M., 2014. Dynamic triggering of deep earthquakes—a global perspective. Abstract S32B-08 presented at the annual AGU meeting, San Francisco, 15-19 Dec.